NASA-CR-193152

NAGW 3037
IN-46-CR
167953
P- 40

The Dynamic Cusp at Low Altitudes: A Case Study Combining Viking, DMSP, and Sondrestrom Incoherent Scatter Radar Observations

Jurgen Watermann and Odile de la Beaujardière
SRI International, Menlo Park, U.S.A.

Dirk Lummerzheim
Geophysical Institute, University of Alaska, Fairbanks, U.S.A.

Joachim Woch
Swedish Institute of Space Physics, Kiruna, Sweden

Patrick T. Newell and Thomas A. Potemra
Applied Physics Laboratory, Johns Hopkins University, Laurel, U.S.A.

Frederick J. Rich
Phillips Laboratory, Hanscom Air Force Base, Hanscom, U.S.A.

Mans Shapshak
Alfvén Laboratory, Royal Institute of Technology, Stockholm, Sweden

short title:
WATERMANN ET AL.: LOW-ALTITUDE DYNAMIC CUSP OBSERVATIONS

(NASA-CR-193152) THE DYNAMIC CUSP AT LOW ALTITUDES: A CASE STUDY COMBINING VIKING, DMSP, AND SONDRESTROM INCOHERENT SCATTER RADAR OBSERVATIONS (SRI International Corp.) 40 p

N93-28842

Unclas

G3/46 0167953

Introduction

The magnetospheric cusps occupy a relatively small part of the magnetosphere but play an important role in the transfer of magnetic flux, plasma, and energy from the solar wind into the magnetosphere. Crooker (1988) considers the cusps topologically as earthward mapping of the dayside merging line between the interplanetary magnetic field (IMF) and the geomagnetic field. The ionospheric footprint of the cusp would coincide with a large electric potential gradient across the high-latitude plasma convection throat. Lockwood and Smith (1989, 1990) consider the cusps merely a series of flux transfer events (FTE), which lead to bursts of magnetosheath plasma injection into the magnetosphere. This idea is further elaborated by Lockwood and Smith (1992) and Smith *et al.* (1992). However, these concepts are difficult to verify unless coincident high and low altitude observations on the same field lines are available.

From a strictly observational standpoint, the cusps can be viewed as the flux tubes where the spectral characteristics of electron and ion precipitation are closer to those of the magnetosheath plasma than anywhere else in the magnetosphere (Newell and Meng, 1988). Because this definition is based on observables it can immediately be used in practice without making assumptions on the plasma transfer processes, e.g. the steadiness or patchiness of the magnetosheath-like particle flux. Therefore we will adhere to this conceptual definition. When using the term "cusp" in this paper we mean the particle cusp as it would be identified from charged particle observations made from low- and mid-altitude spacecraft such as DMSP and Viking (Newell and Meng, 1988; Kremser and Lundin, 1990; Aparicio *et al.*, 1991).

Because the location and size of the cusp for the state and dynamics of the magnetosphere are so important, a ground-based sensor capable of detecting and monitoring the cusp or its ionospheric footprint would be valuable. To suggest and demonstrate a possible method is the purpose of this paper. By calibrating ground-based incoherent scatter radar observations with space borne particle measurements, we determine the signature of

the particle cusp. Once this is done we monitor with the radar its temporal evolution, i.e. its dynamic behavior. Such intercalibration provides the opportunity to add the time or longitude dimension to the latitudinal extent of the cusp which is normally obtained from *in-situ* spacecraft measurements.

Utilization of a high-latitude incoherent scatter radar to monitor the cusp constitutes only one of several possible approaches. Others include observation of auroral emissions (Sandholt *et al.*, 1985; Sivjee, 1985; McEwen, 1985), categorization of backscatter from coherent HF radars (Baker *et al.*, 1990), examination of magnetic pulsation characteristics (Engebretson *et al.*, 1986; Olson, 1986), correlation studies between optical emissions and geomagnetic pulsations (McHarg and Olson, 1992), and observation of VLF signal characteristics and cosmic noise absorption (Engebretson *et al.*, 1990).

In this paper we present a case study involving data from three satellites and a ground-based radar. We focus on a detailed discussion of observations of the dynamic cusp made on 24 September 1986 in the dayside high-latitude ionosphere and interior magnetosphere. In the next section we present the relevant data from space-borne and ground-based sensors. They include *in-situ* particle and field measurements from the DMSP-F7 and Viking spacecraft and Sondrestrom radar observations of the ionosphere. These data are augmented by observations of the IMF and the solar wind plasma. We compare the observations with predictions about the ionospheric response to the observed particle precipitation, obtained from an auroral model. We show that observations and model calculations fit well and provide a picture of the ionospheric footprint of the cusp in an invariant latitude versus local time frame. The combination of Viking, Sondrestrom radar, and IMP-8 data suggests that we observed an ionospheric signature of the dynamic cusp. We were able to monitor its spatial variation over time which appeared closely related to the variation of the southward component of the IMF.

Spacecraft Observations

During a GISMOS/Sundial experiment on 24 September 1986, the Sondrestrom incoherent scatter radar (Kelly, 1983) was operated in a mode that consisted of an antenna elevation scan perpendicular to the local L shell, followed by a sequence of measurements with various fixed antenna positions. This cycle was repeated every 25 minutes. For details of this so-called World Day mode see Watermann *et al.* (1993), who describe another radar experiment with an antenna mode which did not differ significantly from the one used here. We first discuss the DMSP data, then the radar data between 9 UT and 19 UT (about 7 to 17 magnetic local time, MLT).

Between 1242:00 and 1245:30 UT, DMSP-F7 moved through the dawnside part of the Sondrestrom radar field of view. In Fig. 1 we have mapped its trajectory on a geographic grid down to 120 km altitude (from 830 km, the satellite altitude). The markers along the trace indicate full minute time intervals. The trace is subdivided into three sections labeled CPS, BPS, and PM. The classification by Newell et al. (1991) is adopted, and the terms were chosen because DMSP-F7 observed in these regions particle precipitation characteristic of the central plasma sheet (CPS), the boundary plasma sheet (BPS), and the plasma mantle (PM). The particle data are shown in Fig. 2 which will be discussed further below. We do not claim that the former two precipitation regions map necessarily to the central and boundary plasma sheets in the tail, instead the particles may have drifted considerably while retaining their original spectral characteristics. The Sondrestrom radar location (SSF) and the trace of the antenna elevation scan at 120 km altitude (heavy line) and 350 km altitude (thin line) are also drawn. Contours of equal invariant latitude, evaluated at 120 km altitude, are overlaid on the geographic grid as dotted lines. The radar covers the *F* region from about 68° to 80° invariant latitude, which provides the opportunity to observe the cusp footprint more often than other existing incoherent scatter radars. Newell and Meng (1992) inferred from an examination of several years of DMSP data that the highest probability to observe the cusp exists in the vicinity of 78° PACE magnetic latitude, which deviates only a fraction of a degree from invariant latitude (see Baker and Wing (1989) for a description

of the PACE coordinate system). Aparicio *et al.* (1991) found the highest percentage of Viking cusp crossings between 78° and 82° invariant latitude.

The DMSP particle precipitation observations made on this pass are shown in Fig. 2. Tick marks with Universal Time and invariant latitude are drawn along the bottomside abscissa, and the precipitation regions, CPS, BPS, PM, and PC (polar cap precipitation) are indicated. The PC region lies poleward of the radar field of view and therefore does not appear in Fig. 1. The top panel shows the electron and ion energy fluxes between 31 eV and 31 keV (the DMSP spectrometer range), in black and orange, respectively. The ordinate is scaled logarithmically, and the unit is eV cm^{-2} s^{-1} sr^{-1}. The second panel shows the average energy of the particle flux measured between 31 eV and 31 keV, the unit is eV. The third panel shows the electron energy spectra (eV cm^{-2} s^{-1} sr^{-1} eV^{-1}) in a color-coded representation, red means highest and violet lowest intensity, white areas mean no counts above the noise level. In this panel energy increases upward along the ordinate. The ion spectra are displayed in nearly the same way in the bottom panel, however, the ordinate is reversed, energy increases toward the bottom. Note that the scaling is different for electrons and ions, the same color in the spectrograms represents different intensities, and there is also an offset between the electron and ion scales in the top panel.

Based on the spectral characteristics of the measured electron and ion precipitation the identification of CPS, BPS, PM, and PC as marked in Fig. 2 appears to be a reasonable interpretation. The BPS electron precipitation is characterized by high intensity and moderate but fluctuating average energy. For our model calculations we will use a spectrum which represents an average over the central, most intense section of the highly structured BPS precipitation.

Half an hour later Viking appeared on field lines which map down into the radar field of view. This spacecraft made observations under orbital conditions significantly different from those pertinent to the DMSP satellite. DMSP-F7 moved in a sun-synchronous circular orbit and was three-axis-stabilized. Therefore its particle spectrometer received only

particles precipitating in the Nadir direction. Viking was spin-stabilized and orbited in a near-cartwheel mode in a highly elliptic orbit. At the time of the observations Viking was about 2 earth radii above the ground. Its cartwheel mode allows pitch angle resolved particle measurements which facilitate the identification of the origin regions of the observed particles.

Fig. 3 shows the 120 km altitude footprint of the Viking pass, in a way similar to Fig. 1. Viking entered the radar field of view dawnward of the antenna scan plane at 1310 UT and left it shortly before 1350 UT, see the UT markers along the trace. Note that both the DMSP and the Viking trajectories intersect the contours of constant invariant latitude almost at a right angle, parallel to the radar scan plane (at least in the poleward section of the radar field of view which is most relevant to this study). In the next two figures we show Viking particle flux observations. We will see that Viking remained within the ring current population until 1335:50 UT, at which point a rapid transition to the cusp proper was observed. The reason for labeling the cusp "dynamic" will become clear further below when we discuss the related radar data. After a short weakening of the precipitation, Viking encountered at 1342:20 UT a second, weaker onset of cusp precipitation which we labeled boundary cusp.

Viking electron flux measurements from the first half of its pass through the radar field of view are shown in Fig. 4. Displayed are uncalibrated electron counts in four energy channels between 8 keV and 37 keV. In the top of the box we have drawn the pitch angle variation, with 0° (inflowing particles) at the topside and 180° (outflowing particles) at the bottomside of the pitch angle trace. One full satellite spin is completed in about 11 seconds. The electron flux plotted to the left of the heavy vertical bar is characterized by a double loss cone distribution which is typical for the ring current population. At 1335:50 a rapid change occurs, the intensities drop substantially, and the double loss cone distribution disappears. At this point, Viking leaves the ring current region and encounters magnetosheath-like plasma. The bursts (more distinct in the lower than in the higher energy channels) represent mainly the high-energy tails of intense bursts of low average energy. A

typical steady-state transition from the ring current region into the low-latitude boundary layer (LLBL) would be characterized by a gradual change of the flux intensity and a degradation of the double loss cone distribution over a few spin periods. Such a signature is entirely missing, therefore we suggest that we observe a transient feature, with the LLBL being completely wiped out, rather than a steady-state situation. This interpretation is the reason behind our choosing the term "dynamic cusp".

The Viking observations for the time period following that of Fig. 4 are displayed in Fig. 5. The format is similar to the DMSP-F7 display (Fig.2), except that now both electrons and ions are plotted with energy increasing upward. The electron and ion energy flux intensities (in eV cm^{-2} s^{-1} sr^{-1} eV^{-1}) are color coded, and the pitch angle variation is plotted along the bottom (but in a sense opposite to that in Fig. 4). The sharp electron flux cutoff near 200 eV is due to the particular observation mode used during this time, it does not imply that no electrons with lower energy existed. One notices two precipitation regimes, separated by the vertical bar between dynamic cusp and boundary cusp. This separation is not as striking as the one between ring current and cusp precipitation. We nevertheless choose to distinguish between the two parts because the boundary cusp starts with a new onset, and the evolution of the ion flux appears like a weak reprise of the dynamic cusp.

Fig. 5 overlaps with Fig. 4 in the time interval 1336-1338 UT. The main differences between the distributions seen in Fig. 5 and in Fig. 4 are the much lower electron average energy and the electron pitch angle isotropy in the cusp region. Note that in this figure the scales for the electron and ion energy flux intensities differ by two orders of magnitude. A large difference between electron and ion precipitation is typical; Hardy *et al.* (1989) have shown that on average the ion energy flux intensity along the noon-midnight meridian is an order of magnitude below that of the electron energy flux at all levels of geomagnetic activity. This has significant implications for the ionospheric effects of particle precipitation. In most cases we will observe only modifications of the ionospheric plasma distribution caused by the electron precipitation, the effect of ion precipitation will hardly be seen.

The average energy of the ions in the cusp region is higher than what would normally be expected in a steady-state cusp. We suggest two explanations. First, the solar wind speed measured by IMP-8 between 12 and 14 UT was much higher than average, it exceeded 600 km/s. Second, if we assume transient field line merging between the IMF and the magnetospheric field, with associated solar wind plasma entry into the magnetosphere, the ions (originating from the magnetosheath) may experience post-acceleration when the merged field lines are draped over the earth towards the magnetotail. If we view this event as a transient phenomenon, the decrease of the average energy of the 0° pitch angle cusp ions between 1337 and 1342 UT should be interpreted as a true time of flight effect, rather than a steady-state velocity filter effect as described by Shelley *et al.* (1976) and Reiff *et al.* (1977). The V-shaped ion pattern suggests a limited spatial extent of the plasma injection region (Burch *et al.*, 1982). Temporally coincident IMF and Sondrestrom radar data shown further below support our suggestion.

We have computed three different electron energy spectra representative for some of the Viking and DMSP measurements. One is an average over several spectra measured by Viking between 1340 and 1341 UT, in the center of the dynamic cusp. The next is an average over the DMSP-F7 measurements between 1244:13 and 1244:54, in the center of the BPS region. The third is a 4-s average over the most intense low energy electron precipitation measured by DMSP-F7 between 1244:27 and 1244:30 UT. These three spectra are plotted together in Fig. 6. The Viking spectrum plotted here is valid for the DMSP altitude. For our model calculations we have extrapolated the Viking spectrum down to 30 eV (the lower limit of the DMSP spectrometer) in a somewhat arbitrary fashion using a slope similar to the mean slope of the DMSP average spectrum below 200 eV. The Viking and DMSP spectra plotted in this figure will provide one basic input parameter to our model simulation, the topic of the next section.

Model Predictions

The DMSP-F7 and Viking average spectra from the central parts of the BPS and the dynamic cusp, respectively, were used as input to an auroral model (Lummerzheim, 1987) to predict the ionospheric response to the measured soft electron precipitation. The model consists of two major parts, one describes the transport of energetic particles and the resulting excitation and ionization processes, and the other deals with the thermospheric chemistry and diffusive transport along the field lines. The major ionization sources considered in the model include electron precipitation, solar EUV radiation, and photoelectrons. The MSIS-90 thermosphere model (Hedin, 1991) provides for a neutral atmosphere, which we modified by reducing the atomic oxygen density to half of its MSIS value. At least for the *E* region the MSIS model has been found to overestimate the atomic oxygen abundance during times of auroral precipitation, e.g. Lummerzheim *et al.* (1990). The ion chemistry reaction rates implemented in the model are those given in the appendix of Rees (1989). The contribution of the ion precipitation to the modification of the ionosphere is neglected because of its relatively low intensity. The model in its current implementation is one-dimensional, i.e. it does not take into consideration horizontal diffusion and convection. It does, however, allow for a pitch angle dependence of the electron flux, a feature which we cannot make use of in this case because the cusp electron flux is almost perfectly isotropic, see Fig. 5.

In our model simulation we assumed that steady soft-electron precipitation along the field line through Sondrestrom (67° geographic latitude) commenced at 0900 solar local time (SLT), corresponding to 1220 UT at Sondrestrom, lasted for 1.5 hours. In two different model runs, the BPS electron flux measured by DMSP-F7 and the dynamic cusp spectrum measured by Viking were used as input parameters. Figs. 7a and 7b show the resulting plasma density and electron and ion temperature distributions in an altitude versus SLT frame. Below the low energy cutoff at 30 eV we had to assume spectral distributions. Examination of different forms of extrapolation of the measured spectra revealed that the modeled ionospheric plasma density distribution is almost insensitive to the form of the

extrapolation to low energies, but the plasma temperatures above some 300 km altitude may change. The model output is therefore only qualitatively valid at altitudes above some 300 km.

Two components dominate the plasma distributions: the effect of solar radiation which varies slowly over local time, and the effect of the temporally limited soft-electron precipitation. Fig. 7a indicates that the DMSP-F7 average BPS spectrum affects the ionosphere very little. Modifications are seen predominantly in the *E* region plasma density, between 120 and 150 km. Only small deviations from the background *F* region plasma densities and the *E* and *F* region plasma temperatures are noticeable. If the model is correct, the changes in the ionosphere are so minor that we do not expect to observe with the radar an effect of the BPS electron precipitation in the *F* region. We cannot verify the predicted plasma density enhancement in the *E* region because the BPS precipitation was detected mainly poleward of the radar *E* region field of view (see Fig. 1).

When the Viking spectrum is taken as input, the model results look strikingly different, as Fig. 7b demonstrates. The plasma density is significantly enhanced throughout the ionosphere, at all altitudes. Below some 300 km it rises immediately and reaches saturation after less than one hour while the response at higher altitudes is delayed for several minutes and has also a longer rise time. The electron temperature shows an increase at altitudes as low as 140 km, and it is substantially elevated above 170 km. The temperature response to the electron precipitation is immediate, from one simulation time step to the next. Saturation is reached after less than one hour, and the *F* region temperature falls back to normal within 1.5 hours after the precipitation is switched off, a time scale similar to the plasma density recovery. The ion temperature also increases, mostly in the upper ionosphere, above 400 km.

Note, however, that our model is one-dimensional. It predicts the effect of electron precipitation on the plasma density and temperatures but does not account for plasma

convection and Joule heating. In other words, when simulating the response of the ionospheric plasma, we assume that the transport of plasma into and out of the precipitation region is negligible.

Incoherent Scatter Radar Observations

We now present the data from several hours of Sondrestrom incoherent scatter radar operation before, during and after the DMSP-F7 and Viking passes shown above. Fig. 8 shows density profiles obtained from two consecutive elevation scans. The upper panel shows measurements from a radar scan performed between 1326:15 and 1331:14 UT (when Viking observed ring current particles), the lower panel measurements from the following scan, performed between 1344:22 and 1349:21 UT (when Viking traversed the boundary cusp). Between these two scans, the antenna was in a multiposition mode. The plasma density, averaged over 20 s, is plotted in an altitude versus invariant latitude frame, with darker shades meaning increased plasma density. One notices the highest plasma density between 200 km and 350 km altitude. The *F* region plasma in the equatorward part of the radar field of view was probably produced by solar radiation and subsequently drifted poleward. This will become more obvious once we discuss Fig. 9. The localized plasma density enhancement, extending from about 75° to 78° invariant and covering the 150 to 400 km altitude range, results most likely from intense soft electron precipitation. This structure coincides with the dynamic cusp detected by Viking.

We examined *F* region plasma density and temperature measurements in order to identify the cusp and distinguish it from the photo-ionization component of the plasma. The plasma temperatures were measured at altitudes of 175, 230, 285, 340, 395 and 450 km. Fig. 8 suggests that the altitude of 285 km is a good representation of the *F* region plasma distribution. The three parameters, plasma density (corrected for Debye length and temperature effects), electron temperature, and ion temperature, evaluated at 285 km altitude, are displayed in Fig. 9 in a stacked clock-dial format. Time runs along the half-

circle, with magnetic noon at the top, and invariant latitude increases from 68° to 80°. Note that this figure is not a snapshot but a composition of a series of elevation scans along the magnetic meridian. The plasma densities and temperatures are gray-shaded in a linear scale, each step represents an increase of $2 \cdot 10^{10}$ m^{-3} in plasma density and 200 K in temperature, respectively. The plasma density exceeds $1.75 \cdot 10^{11}$ m^{-3}, the electron temperature 2700 K, and the ion temperature 1900 K, in the darkest areas.

Between 1000 and 1200 MLT (1200 - 1400 UT) the density distribution (N_e) shows the noon-sector plasma tongue. Two cross sections within the region of increased density were plotted in Fig. 8. The equatorward part of this tongue is characterized by relatively low electron and ion temperatures. The low electron temperature indicates that the region of increased N_e consists of plasma which had enough time to cool down, meaning that the neutral gas was ionized some time before. The highest electron densities and temperatures were measured in the poleward section of the region of increased density, within a limited area extending over 1.5 hours local time and two degrees invariant latitude. Note that these density and temperature increases are small—they amount to only 20%.

To enhance the visibility of this plasma structure we have replotted the 285 km altitude clock dial of Fig. 9 but changed the intensity scale. Fig. 10 shows the same data as Fig. 9, but this time we have filled the area where both the electron density and temperature exceeded $1.75 \cdot 0^{11}$ m^{-3} and 2500 K, respectively. We have left blank all the other areas where only one or none of these two requirements were fulfilled. We have also included the downward projected trajectories of DMSP-F7 and Viking and indicated by a dotted trajectory segment the dynamic cusp as detected by Viking. Except for two spurious small spots there is one contiguous area where high electron density and temperature coincide. This figure confirms the prediction of the ionospheric model: enhanced plasma density and elevated temperature in the *F* region are found in the same latitude range where Viking identified cusp electron flux. No such increases are seen at the time of the DMSP pass, and no cusp precipitation was detected by DMSP-F7. The agreement between observations and model predictions demonstrates the usefulness of the model despite its simplicity in certain

aspects. We need to note, however, that the exact spatial extent of the cusp cannot be determined from the radar observations. The thresholds of $1.75 \cdot 10^{11}$ m^{-3} and 2500 K for electron density and temperature are somehow arbitrary and were chosen because they safely exceed the average background numbers but remain below the peak values. A higher or lower threshold would lead to a decrease or increase in the size of the filled area in Fig. 10.

Data Interpretation

Once we have calibrated, at least qualitatively, the radar observations with the spacecraft measurements, we can use the radar to monitor the evolution of the cusp. In this event, for instance, we notice that the radar observed a cusp signature over about 1.5 hours local time. With time progressing, the cusp tended to move to lower latitudes, which is clearly seen in Figs. 10 and 11. While Fig. 10 displays the radar elevation scan data in a continuous fashion, achieved by smoothing and interpolation, Fig. 11 (lower panel) displays the radar data without filling in during the time periods when the radar was performing a multiposition cycle. We have used the same electron density and temperature thresholds as in Fig. 10 and plotted in an invariant latitude versus Universal Time frame those sections of the elevation scans where the thresholds were exceeded. The Viking cusp traversal fell exactly between two scans.

Above the radar data we have added a panel showing the IMF variation over this period. IMF data are available only from 1200 UT onward. We have plotted them with a 10 min delay to account for the IMF travel time between the location of IMP-8 and the bow shock front and the propagation of the IMF through the bow shock. Each of them are estimated to take about five minutes. Interplanetary plasma data are available only during the interval 1210 to 1340 UT, and the plasma parameters changed only slightly during this interval. The solar wind speed increased steadily from some 600 km/s to about 640 km/s, the proton density remained stable at about 3.5 cm^{-3}, and the plasma temperature

fluctuated moderately around an average of 95,000 K. The IMF was rather weak, and its total intensity remained stable at 5 nT, as Fig. 11 shows. B_y stayed around -2.5 nT, except between 1230 to 1045 UT when it changed sign for a brief instant. The most significant variations occurred in B_z which changed sign several times during the 1200-1500 UT interval.

It is interesting to note that the variation of the cusp latitude as seen by the radar seems to be correlated with the IMF-B_z variation. The more negative B_z grows the more equatorward the cusp moves, and vice versa. Because of the small changes in the interplanetary plasma parameters we exclude the effect of solar wind dynamic pressure variations on the cusp latitude. Such pressure changes were suggested by Potemra *et al.* (1992) to explain Viking observations from 6 September 1986, made at the same local time and invariant latitude as those in our paper, in terms of a poleward retreating cusp. The question arises whether the radar simply scanned a steady-state cusp located more equatorward at its duskward than at its dawnward edge, or whether the radar monitored a temporal variation of the cusp location. We suggest that the latitudinal variation of the cusp is a temporal rather than a spatial effect, therefore we have used the term "dynamic cusp" in this paper.

A dynamic nature of magnetosheath particle injection into the magnetosphere was also suggested by Lockwood and Smith (1989) to explain DE-2 observations of low-energy ion fluxes (along with imager and magnetometer observations) in terms of a growing region of newly merged field lines. Such an event would be observed as an equatorward propagating region of magnetosheath-like precipitation as is normally found in the cusp. However, they associated their observations with a flux transfer event (FTE) rather than a dynamic cusp.

A statistical analysis conducted by Newell *et al.* (1989) showed that the equatorward boundary of the cusp changes very little between about 11.5 and 12.5 MLT in the case of positive B_x and negative B_z, see the dashed line in their Fig. 4b. On the other hand, their Fig. 5a indicates that for southward IMF the equatorward boundary of the cusp is detected at lower latitudes if B_z becomes more negative. It is likely that we see such an IMF-B_z

dependence of the cusp in Fig. 11. Based on the combined radar and spacecraft observations we conclude that the extent in latitude and local time, the size, and the correlation of the equatorward and poleward boundaries of the region of soft-electron precipitation and increased *F* region electron density and temperature with the IMF-B_z support the idea of a dynamic cusp more than that of an FTE. We conclude further that the results of Newell *et al.* (1989) are not only valid in a statistical sense but also in an individual case when the IMF-B_z component varies over time.

Field-Aligned Currents and Plasma Convection

The existence of a pair of locally confined field-aligned currents in the cusp region had been suggested by Iijima and Potemra (1976) to explain measurements made with the TRIAD satellite. The authors admitted that there is no compelling evidence to believe that these so-called cusp currents are truly distinct from the traditional region 1 and region 2 currents. The controversy continued about the origin of the cusp currents and whether they are distinct from region 1 and region 2 currents, see Saunders (1989), and de la Beaujardière *et al.*, 1993. If a pair of such distinct currents would be characteristic for the cusp, one could use their signature to identify the cusp location. Recently, de la Beaujardière *et al.* (1993) demonstrated that the transitions between upward and downward field-aligned currents do not in general coincide with the boundaries of magnetospheric regions inferred from space-borne particle precipitation measurements.

To determine if the field-aligned currents might help to distinguish the cusp from other magnetospheric regions we examined the magnetometer data acquired onboard the satellites. The magnetic perturbation vectors along the DMSP-F7 and Viking trajectories in the plane perpendicular to the geomagnetic field are plotted in Fig. 12a and 12b, respectively. The spacecraft flight history proceeds from low to high latitudes from the left to the right margin of the figure. Vectors pointing to the top margin of the panel are directed dawnward, those pointing to the bottom margin are duskward. If one interprets the

magnetic field vectors in terms of field-aligned sheet currents, an increase of the vector length toward the top margin represents an upward current, and a decrease (or increase toward the bottom margin) a downward current.

The DMSP-F7 magnetic field data, Fig. 12a, show the signature of an upward current which begins to show a magnetic effect while the satellite is still in the CPS region. This upward current continues across the CPS/BPS boundary and into the BPS region where the current changes orientation to become a downward current extending into the PM. Within the PM and well poleward of the BPS/PM boundary the current again changes orientation several times, but over short distances. The average intensities of the main sequence of upward-downward currents are 0.3 and 0.6 μA m^{-2}. These are probably the region 2 and region 1 currents. There is obviously no coincidence between magnetospheric boundaries (based on particle precipitation characteristics) and changes in the orientation or intensity of the field-aligned currents, a result consistent with de la Beaujardière *et al.* (1993).

The Viking magnetometer data are plotted in Fig. 12b, in a way similar to Fig. 12a, except that the averages are now taken over 18 s, instead of 5 s as in the case of DMSP-F7. Different smoothing window lengths were chosen to compensate for the different orbital velocities. Before 1330 UT a brief interval of small magnetic perturbation (i.e. field-aligned current) is noticed; this occurs well within the ring current region. Shortly before Viking leaves the ring current region and enters the cusp, a dawnward magnetic perturbation, indicative of an upward current, is seen. The magnetic perturbation vector rotates shortly after Viking passes the equatorward boundary of the dynamic cusp, but clearly within the cusp and not at its boundary. The upward current extends throughout the dynamic cusp and changes orientation at the transition to the boundary cusp. The mean densities of the upward and downward currents are both about 0.4 μA m^{-2}, comparable to the densities measured along the DMSP-F7 trajectory. Once again we are led to conclude that no significant change in intensity or orientation of the field-aligned currents is noticed at the equatorward boundary of the dynamic cusp. Remember the striking discontinuity in particle

precipitation characteristics at this particular boundary (shown in Fig. 4), which leaves no doubt about the exact placement of this magnetospheric boundary.

We conclude that variations of the magnetic perturbation vector and consequently changes in field-aligned sheet currents along the spacecraft trajectories do not in general coincide with the boundaries between different magnetospheric regions. More specifically, observations of the field-aligned currents do not provide for a useful method to determine the cusp.

It was suggested that the footprint of the merging line between IMF and magnetospheric field crosses the plasma convection throat where flux enters the polar cap. This junction is between the morning and afternoon high-latitude convection cells (Crooker, 1988). If we assume that magnetosheath-like particles enter the magnetosphere along the merged field lines, then this convection throat would be the locus of the particle cusp. Unless one assumes a steady-state convection pattern, it is almost impossible to identify the convection throat solely from measurements made with a scanning radar or a single spacecraft, because they sample only a cross section at a given time. Instead, one needs a true two-dimensional snapshot of the convection pattern. The event discussed here does by no means represent a steady-state situation, and we cannot really apply the convection throat criterion. In the next section we will point out, however, that neither the Viking nor the radar electric field and plasma drift observations clearly indicate the presence and location of the cusp and thus can resolve this issue. Although Crooker's model of the merging line (i.e. the cusp) mapping to the plasma convection throat makes sense theoretically, there seems to be little chance to use it in practice with an incoherent scatter radar.

Discussion and Conclusion

The main results obtained from Viking and Sondrestrom radar measurements are graphically summarized in Fig. 13. We use the same grid as in Fig. 3 and have added some of the observed features to it. Along the footprint of the spacecraft trajectory we have indicated by solid arrowheads the actual locations of the Viking footprint when the IMF-B_z component changed sign (10 min delay included). We have also indicated where the onboard magnetometer detected upward ($\odot$) and downward ($\otimes$) field-aligned currents. Further on, the Viking trace serves as the foot of vectors pointing mostly to the right (with three exceptions). These vectors represent the $\boldsymbol{E}\times\boldsymbol{B}$ plasma drift inferred from the spin-plane component of the measured electric field. Viking span in a near-cartwheel mode, the angle between spin plane and trajectory being only 17°. Although these drift vectors show only one component and are therefore of limited value, they indicate that the plasma drift did not reverse within the interval plotted. No significant changes are noticeable at the boundary between ring current region and cusp. The drift components reach their maximum values near the transition from dynamic cusp to boundary cusp.

The radar scan trace is likewise enhanced with a display of results from radar observations. We have cross-hatched the interval between 75.5° and 77.5° invariant latitude where the radar detected an *F* region structure with above-background electron density and temperature. Also plotted along the scan trace are the plasma drift vectors inferred from radar measurements. Because of the 25-min radar cycle time, radar velocity measurements were made up to 12 minutes before or after the spacecraft crossed the same *L* shell. We therefore interpolated the radar measurements made on a given *L* shell to the time when Viking crossed the same *L* shell. In the central part of the radar scan, where *E* region measurements are available, we inferred the drift vectors in two different ways. One method makes use of the altitude dependence of the ratio between Hall and Pedersen ion mobilities and therefore requires *E* and *F* region measurements (for details see de la Beaujardière *et al.*, 1977). The other method uses pairs of fixed positions with different antenna azimuths,

and combines data from each position pair with data from a field-aligned antenna position in order to derive velocity vectors. This method requires only *F* region measurements and thus covers a wider latitude range. Outside the interval 72.0° to 75.5° invariant latitude we can construct plasma velocity vectors with the latter method only.

At latitudes below the equatorward boundary of the cusp footprint (75.5° invariant) we find small north-westward (poleward-dawnward) velocities of less than 1000 m/s which fluctuate very little. The two methods give consistent results over the range where both are applicable. In the cusp region the vector orientations change sign from one latitude step to the next, but here we can build only on the multiposition method and have no confirmation from the other method. Therefore it remains unclear whether the fluctuating drift orientation is physically significant or instead a result of data noise, large velocity uncertainties, or temporal variations. A hint toward physical explanation may be seen in coherent HF radar backscatter observations from the cusp region. Baker *et al.* (1990) found a significantly increased level of plasma irregularity turbulence in the cusp (probably in the *F* region), resulting in rather broad spectra. If they are associated with a high level of electric field turbulence, the incoherent scatter radar measurements in fixed antenna positions with their typically 30 - 60 s integration time could indeed result in mean velocity estimates largely influenced by a random state of the electric field due to the turbulence. Poleward of the cusp the drift pattern seems to stabilize, and we find consistently duskward-poleward velocities of about 2000 m/s.

We have examined Sondrestrom radar data from several hours during this day as well as from other days, and found that intervals characterized by velocities switching back and forth from dawnward to duskward are not always present but also not uncommon. Therefore we cannot attribute such a pattern solely to the cusp and cannot consider it a reliable signature of the cusp.

An interesting point to mention is the obvious difference between plasma velocities inferred from the Viking electric field experiment and from radar measurements. Although

the Viking data provide only one vector component and thus do not permit detailed comparisons, it is clear that Viking data suggest consistently duskward pointing flow vectors while the radar data suggest consistently dawnward pointing vectors for most of the latitudes covered; only poleward of 78° invariant Viking and Sondrestrom radar show consistently duskward drifts. Given the spatial separation between the Viking trajectory and the radar scan plane, some 8° in longitude (30 minutes in local time), and taking into account the dynamic nature of this event, such difference seems to be possible. The high-latitude noon sector, in particular the vicinity of the cusp, is typically characterized by structures with small temporal and spatial scales.

After all, one feature remains outstanding. It concerns the coincidence between soft, magnetosheath-like electron precipitation and locally increased *F* region electron density and temperature. Similar features appeared in other coincident spacecraft/radar cusp observations which we examined (Watermann *et al.*, 1992). Our analysis thus shows that a ground-based incoherent scatter radar has the potential to monitor the temporal development of the cusp, once the radar cusp signature has been calibrated with space-borne particle precipitation measurements. This opens up the possibility to use an incoherent scatter radar as a sensor for monitoring the cusp over an extended time interval rather than to rely solely on relatively rare spacecraft passes through the cusp region which make *in-situ* measurements only along their trajectories. Continuous radar observations make possible the determination of the dynamic behavior of the cusp.

In this paper we have demonstrated the ability of a ground-based incoherent scatter radar performing continuous antenna scans to follow the temporal and spatial evolution of the cusp. Although the method has shown some success we need to add a word of caution. The particle cusp is identified from a synoptic examination of electron *and* ion spectral characteristics. Because the ion energy flux is in most cases one or more orders of magnitude below the electron energy flux, the ionosphere is not very sensitive to the ions, and all we can distinguish from the background plasma distribution is basically the effect of the electron precipitation. We have found cases when intense low-energy electron

precipitation, typical for magnetosheath plasma, covered a latitude range wider than the cusp and extended into the LLBL and PM (Watermann *et al.*, 1992, 1993). In such situations the radar observations allow to estimate only a maximum cusp extent. We cannot determine the size and location of the cusp proper, except that we know it must be within the somewhat wider region of intense soft electron flux. But even in such cases the radar observations are potentially useful because they do at least pose an upper limit to the width of the cusp.

Acknowledgement. Magnetic field line tracing and calculation of invariant latitudes was performed using FORTRAN routines provided by the National Space Science Data Center. This work was supported by NASA contracts NASW 4603, NAGW 3037; NSF grants ATM 9022197, 9108193, 9112680, 9202795; and NSF cooperative agreement ATM 8822560.

REFERENCES

Aparicio, B., B. Thelin, and R. Lundin, The polar cusp from a particle point of view: A statistical study based on Viking data, *J. Geophys. Res.*, **96,** 14023, 1991.

Baker, K.B., and S. Wing, A new magnetic coordinate system for conjugate studies at high latitudes, *J. Geophys. Res.*, **94,** 9139-9143, 1989.

Baker, K.B., R.A. Greenwald, J.M. Ruohoniemi, J.R. Dudeney, M. Pinnock, P.T. Newell, M.E. Greenspan, and C.-I. Meng, Simultaneous HF-radar and DMSP observations of the cusp, *Geophys. Res. Lett.*, **17,** 1869, 1990.

Burch, J.L., P.H. Reiff, R.A. Heelis, J.D. Winningham, W.B. Hanson, C. Gurgiolo, J.D. Menietti, R.A. Hoffman, and J.N. Barfield, Plasma injection and transport in the mid-altitude polar cusp, *Geophys. Res. Lett.*, **9,** 921-924, 1982.

Crooker, N.U., Mapping the merging potential from the magnetopause to the ionosphere through the dayside cusp, *J. Geophys. Res.*, **93,** 7338-7344, 1988.

de la Beaujardière, O., J. Watermann, P.T. Newell, and F. Rich, Relationship between Birkeland current regions, particle precipitation, and electric fields, *J. Geophys. Res.*, **98,** 7711-7720, 1993.

de la Beaujardière, O., R. Vondrak, and M. Baron, Radar observations of electric fields and currents associated with auroral arcs, *J. Geophys. Res.*, **82,** 5051, 1977.

Engebretson, M.J., B.J. Anderson, L.J. Cahill, Jr., R.L. Arnoldy, T.J. Rosenberg, D.L. Carpenter, W.B. Gail, and R.H. Eather, Ionospheric signatures of cusp latitude Pc 3 pulsations, *J. Geophys. Res.*, **95,** 2447, 1990.

Engebretson, M.J., C.-I. Meng, R.L. Arnoldy, and L.J. Cahill, Jr., Pc 3 pulsations observed near the polar cusp, *J. Geophys. Res.*, **91,** 8909, 1986.

Erlandson, R.E., L.J. Zanetti, T.A. Potemra, P.F. Bythrow, and R. Lundin, IMF B_y dependence of region 1 Birkeland currents near noon, *J. Geophys. Res.*, **93,** 9804-9814, 1988.

Hardy, D.A., M.S. Gussenhoven, and D. Brautigam, A statistical model of auroral ion precipitation, *J. Geophys. Res.*, **94,** 370, 1989.

Hedin, A.E., Extension of the MSIS thermosphere model into the middle and lower atmosphere, *J. Geophys. Res.*, **96,** 1159, 1991.

Iijima, T., and T.A. Potemra, Field-aligned currents in the dayside cusp observed by Triad, *J. Geophys. Res.*, **81,** 5971-5979, 1976.

Kelly, J.D., Sondrestrom radar — initial results, *Geophys. Res. Lett.*, **10,** 1112, 1983.

Kremser, G., and R. Lundin, Average spatial distributions of energetic particles in the midaltitude cusp/cleft region observed by Viking, *J. Geophys. Res.*, **95,** 5753, 1990.

Lockwood, M., and M.F. Smith, Low-altitude signatures of the cusp ad flux transfer events, *Geophys. Res. Lett.*, **16,** 879-882, 1989.

Lockwood, M., and M.F. Smith, Reply, *Geophys. Res. Lett.*, **17,** 305-306, 1990.

Lockwood, M., and M.F. Smith, The variation of reconnection rate at the dayside magnetopause and cusp ion precipitation, *J. Geophys. Res.*, **97,** 14,841-14,847, 1992.

Lummerzheim, D., Electron transport and optical emissions in the aurora, Ph.D. thesis, University of Alaska, Fairbanks, 1987.

Lummerzheim, D., M.H. Res, and G.J. Romick, The application of spectroscopic studies of the aurora to thermospheric neutral composition, *Planet. Space Sci.*, **38,** 67, 1990.

McEwen, D.J., Optical-particle characteristics of the polar cusp, in *The Polar Cusp*, edited by Jan A. Holtet and Alv Egeland, 193-202, Reidel, Dordrecht/Boston/Lancaster, 1985.

McHarg, M.G., and J.V. Olson, Correlated optical and ULF magnetic observations of the winter cusp-boundary layer system, *Geophys. Res. Lett.*, **19,** 817, 1992.

Newell, P.T., and C.-I. Meng, The cusp and the cleft/boundary layer: Low-altitude identification and statistical local time variation, *J. Geophys. Res.*, **93,** 14549, 1988.

Newell, P.T., C.-I. Meng, D.G. Sibeck, and R. Lepping, Some low-altitude cusp dependencies on the interplanetary magnetic field, *J. Geophys. Res.*, **94,** 8921-8927, 1989.

Newell, P.T., S. Wing, C.-I. Meng, and S. Sigillito, The auroral oval position, structure, and intensity of precipitation from 1984 onward: An automated on-line data base, *J. Geophys. Res.*, **96,** 5877-5882, 1991.

Newell. P.T., and C.-I. Meng, Mapping the dayside ionosphere to the magnetosphere according to particle precipitation characteristics, *Geophys. Res. Lett.*, **19,** 609, 1992.

Olson, J.V., ULF signatures of the polar cusp, *J. Geophys. Res.*, **91,** 10055, 1986.

Potemra, T.A., R.E. Erlandson, L.J. Zanetti, R.L. Arnoldy, J. Woch, and E. Friis-Christensen, The dynamic cusp, *J. Geophys. Res.*, **97,** 2835-2844, 1992.

Rees, M.H., *Physics and Chemistry of the Upper Atmosphere*, Cambridge Atmospheric and Space Science Series, Cambridge University Press, 1989.

Figure Captions

Fig. 1 The DMSP-F7 late-morning (9.8 MLT) pass of 24 September 1986, mapped down to 120 km altitude and projected on a geographic grid with superposed contours of equal invariant latitude (dotted). Full minute UT markers and particle precipitation regions are plotted along the satellite trace (CPS = central plasma sheet, BPS = boundary plasma sheet, PM = plasma mantle). The Sondrestrom radar location (SSF) with the antenna elevation scan trace at altitudes of 120 km (thick) and 350 km (thin) are also shown.

Fig. 2 DMSP-F7 measurements of particle precipitation during the pass shown in Fig. 1. Top panel: electron and ion average energies and energy fluxes integrated over the spectrometer energy ranges; middle and bottom panels: electron and ion energy flux spectrograms (31 eV to 31 keV), with the ion panel ordinate reversed.

Fig. 3 The Viking cusp pass of 24 September 1986 (orbit 1181) around 11.0 MLT, mapped down to 120 km and plotted on the same grid as the DMSP-F7 pass in Fig. 1.

Fig. 4 Energetic electron flux measured aboard Viking in the equatorward section of the pass shown in Fig. 3. Particle origin regions, as inferred from their spectral characteristics, are also marked.

Fig. 5 Electron and ion energy flux spectrograms obtained from Viking in the poleward section of the pass shown in Fig. 3. The interval 1336-1338 UT overlaps with Fig. 4.

Fig. 6 Average electron precipitation spectra: (i) from the Viking cusp crossing (between 1340 and 1341 UT); (ii) from 4 seconds of maximum low-energy flux intensity during the DMSP-F7 BPS traversal (labeled max.), and (iii) from all the DMSP-F7 BPS traversal (between 1244 and 1245 UT).

Fig. 7 Altitude distributions of plasma density (top), electron temperature (middle) and ion temperature (bottom) over solar local time, obtained from an auroral model. Input parameters include: (a) the BPS average precipitation observed by DMSP-F7, (b) the cusp precipitation observed by Viking (see Fig. 6), both assumed to be effective between 0900 and 1030 SLT.

Fig. 8 Ionospheric electron density distributions in the radar antenna scan plane (perpendicular to the local L shell), obtained from the scan before (top) and after (bottom) the Viking cusp pass. Most of the *F* region consists of plasma produced by solar photoionization; the enhancement between 75° and 78° coincides with the particle cusp.

Fig. 9 Radar measurements of plasma density (NE, top), electron temperature (TE, middle), and ion temperature (TI, bottom) at 285 km altitude, in a local time versus invariant latitude clock dial. Inner circle scaled in MLT, outer circle in UT, invariant latitude increases from 69° (outer circle) to 80 ° (inner circle). Darkest shades indicate highest densities and temperatures, see broken-off segments of linear gray-shade scales on the right hand side of the clock dials.

Fig. 10 The electron density and temperature distribution shown in Fig.9, replotted with filled areas exceeding both thresholds of $N_e > 1.75 \cdot 10^{11}\,m^{-3}$ and $T_e > 2500$ K. In the blank areas, either the density, or the temperature, or both, remain below these thresholds. The dotted segment on the Viking trajectory indicates the dynamic particle cusp extent as inferred from Figs. 4 and 5. The large filled area is considered the ionospheric footprint of the dynamic cusp.

Fig. 11 Bottom: Plasma density and temperature at 285 km altitude exceeding the thresholds indicated (considered the cusp footprint). Data from individual radar scans, together with the Viking pass (dynamic cusp section heavy). Top: Variation of the IMF measured by IMP-8, plotted with 10 min delay. The latitudinal shift of the cusp footprint is roughly correlated with the variation of the IMF-B_z component.

Fig. 12 (a) 5-s averages of the magnetic perturbation in the horizontal plane (approximately perpendicular to the geomagnetic main field), measured by DMSP-F7 on its polebound pass shown in Fig. 1. (b) 18-s averages of the magnetic perturbation in the plane perpendicular to the geomagnetic main field, measured by Viking on its pass shown in Fig. 3. In both cases, upward pointing vectors are westward (dawnward), downward pointing vectors eastward (duskward) oriented.

Fig. 13 Composite plot of the Viking and Sondrestrom radar observations on 24 September 1986. Figure identical to Fig. 3 but enhanced with indicators of IMF-B_z sign changes (◂), distribution of field-aligned currents (⊙ and ⊗), and $\boldsymbol{E}\times\boldsymbol{B}$ drift (from the spin plane electric field component only) along the Viking trace. Field perpendicular plasma drift vectors from radar measurements and the interval of above-background F region electron density and temperature (cross-hatched) are plotted along the antenna scan trace.

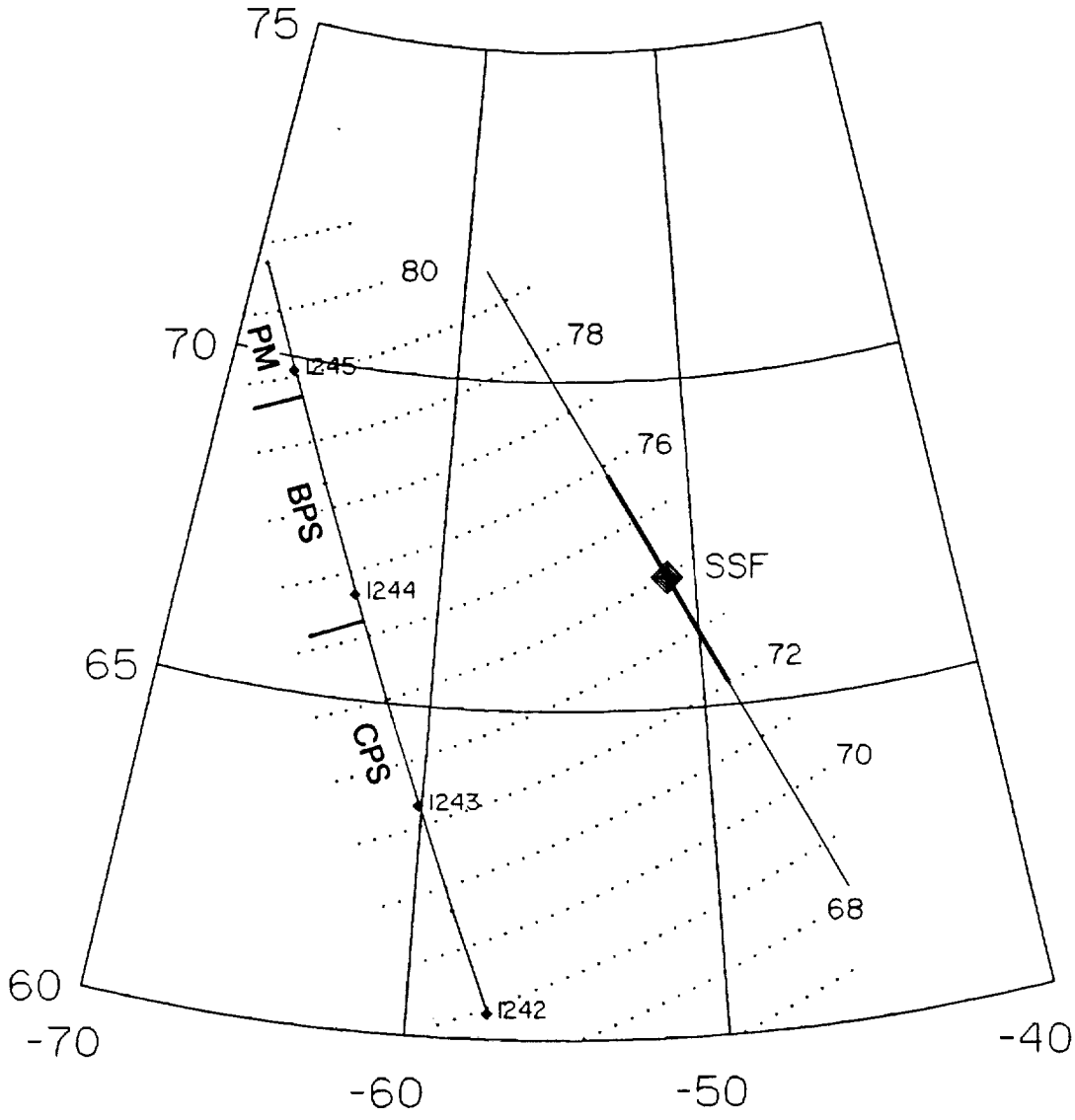
75
70
65
60
-70
-60
-50
-40
80
78
76
72
70
68
PM
1245
BPS
1244
CPS
1243
1242
SSF

Fig. 1

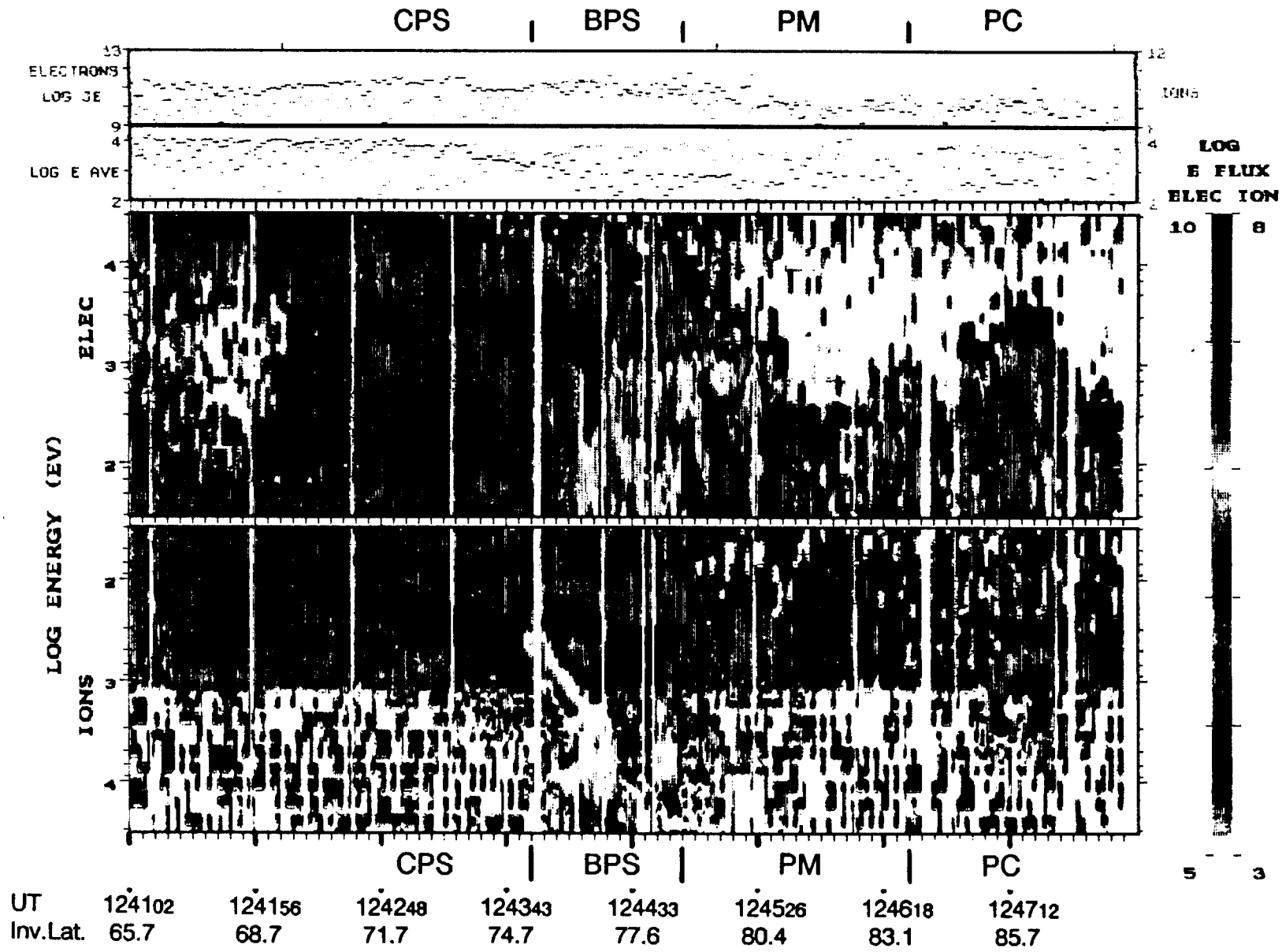
CPS
BPS
PM
PC
ELECTRONS
LOG JE
LOG E AVE
IONS
LOG
E FLUX
ELEC ION
10
8
5
3
ELEC
IONS
LOG ENERGY (EV)
UT
Inv.Lat.
124102
65.7
124156
68.7
124248
71.7
124343
74.7
124433
77.6
124526
80.4
124618
83.1
124712
85.7

Fig. 2

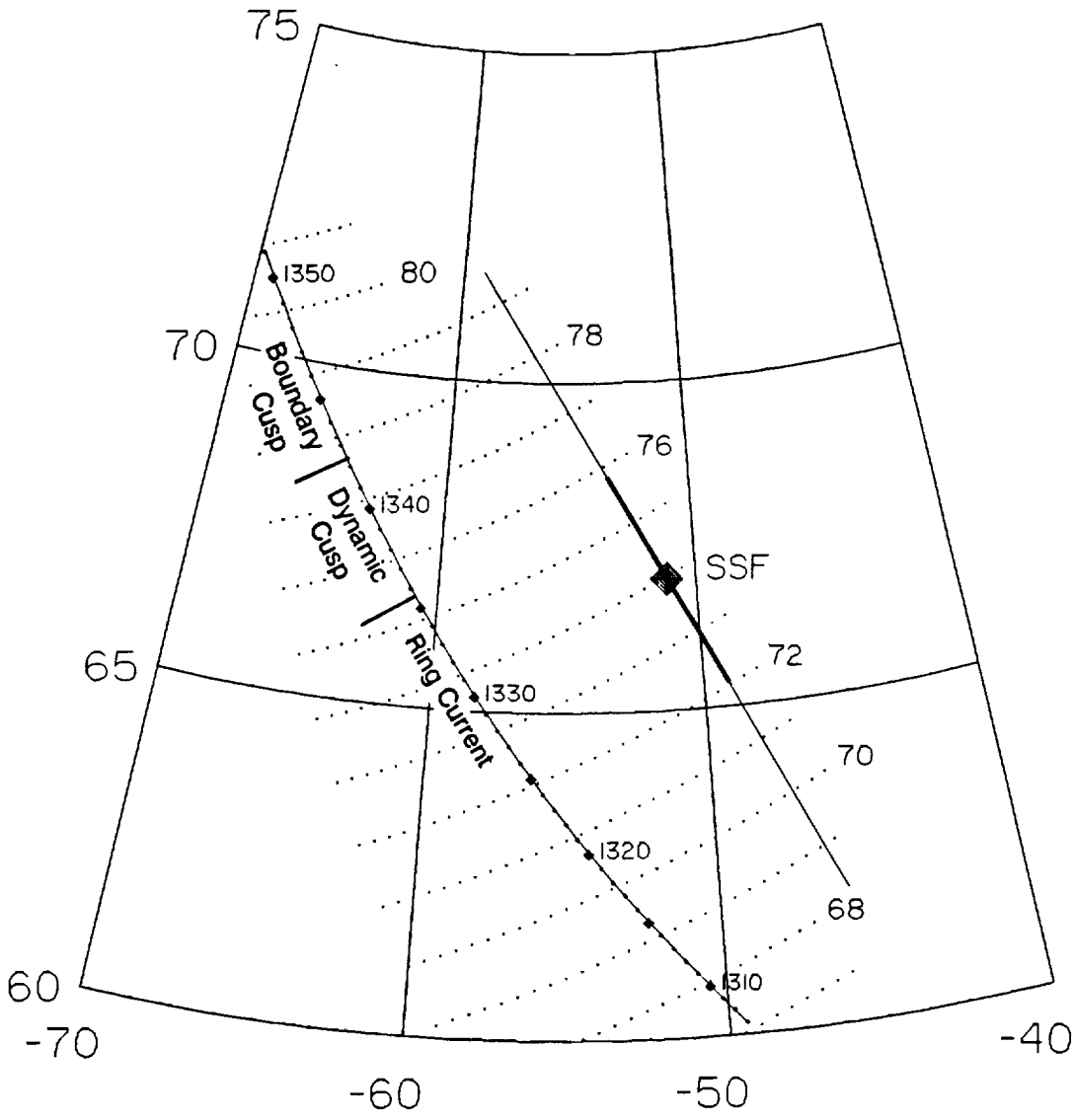
75
70
65
60
-70
-60
-50
-40
1350
1340
1330
1320
1310
80
78
76
72
70
68
Boundary Cusp
Dynamic Cusp
Ring Current
SSF

Fig. 3

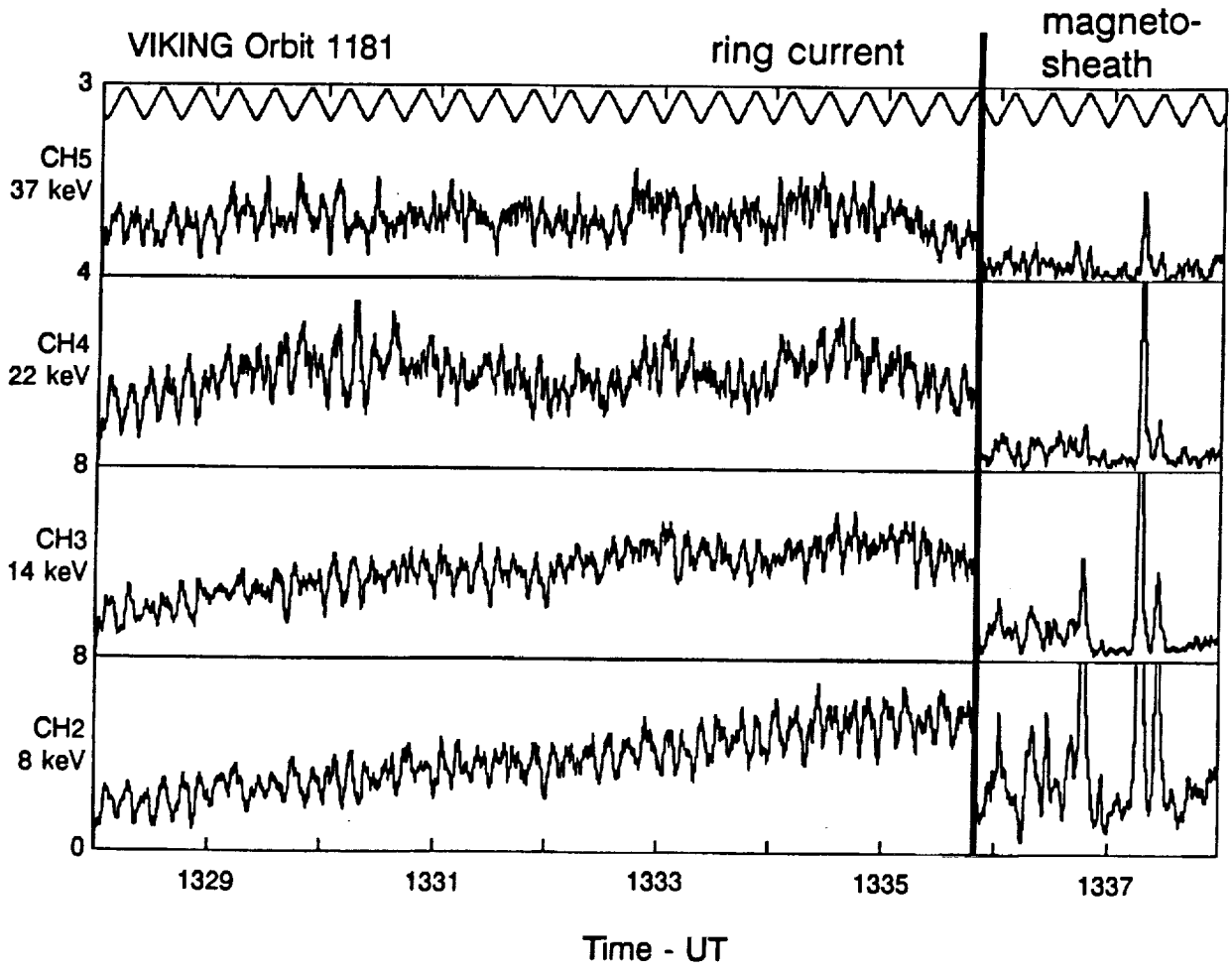
VIKING Orbit 1181
ring current
magneto-
sheath
3
CH5
37 keV
4
CH4
22 keV
8
CH3
14 keV
8
CH2
8 keV
0
1329
1331
1333
1335
1337
Time - UT

Fig. 4

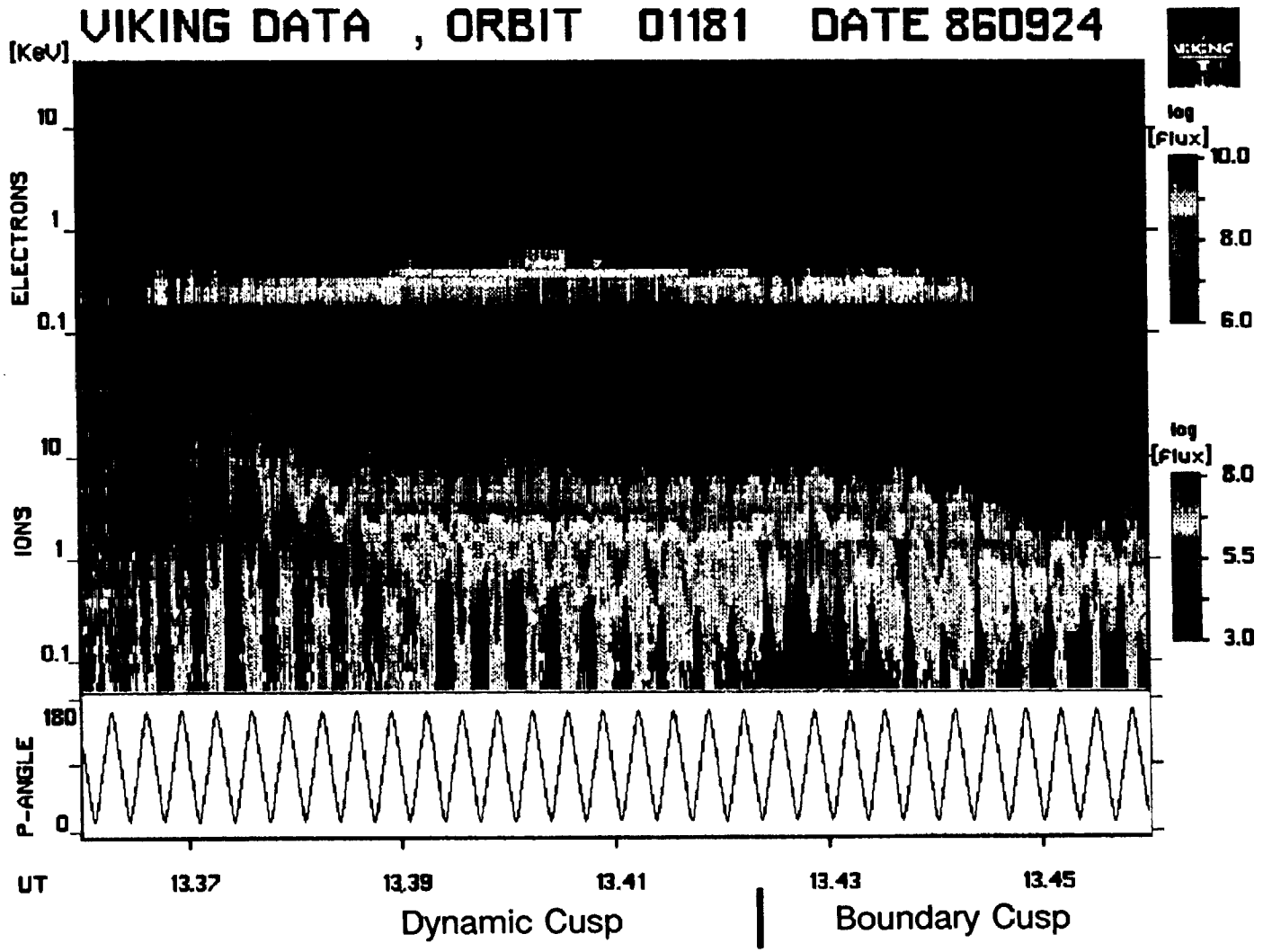
VIKING DATA , ORBIT 01181 DATE 860924
[KeV]
ELECTRONS
10
1
0.1
IONS
10
1
0.1
log [Flux]
10.0
8.0
6.0
log [Flux]
8.0
5.5
3.0
P-ANGLE
180
0
UT
13.37
13.39
13.41
13.43
13.45
Dynamic Cusp
Boundary Cusp

Fig. 5

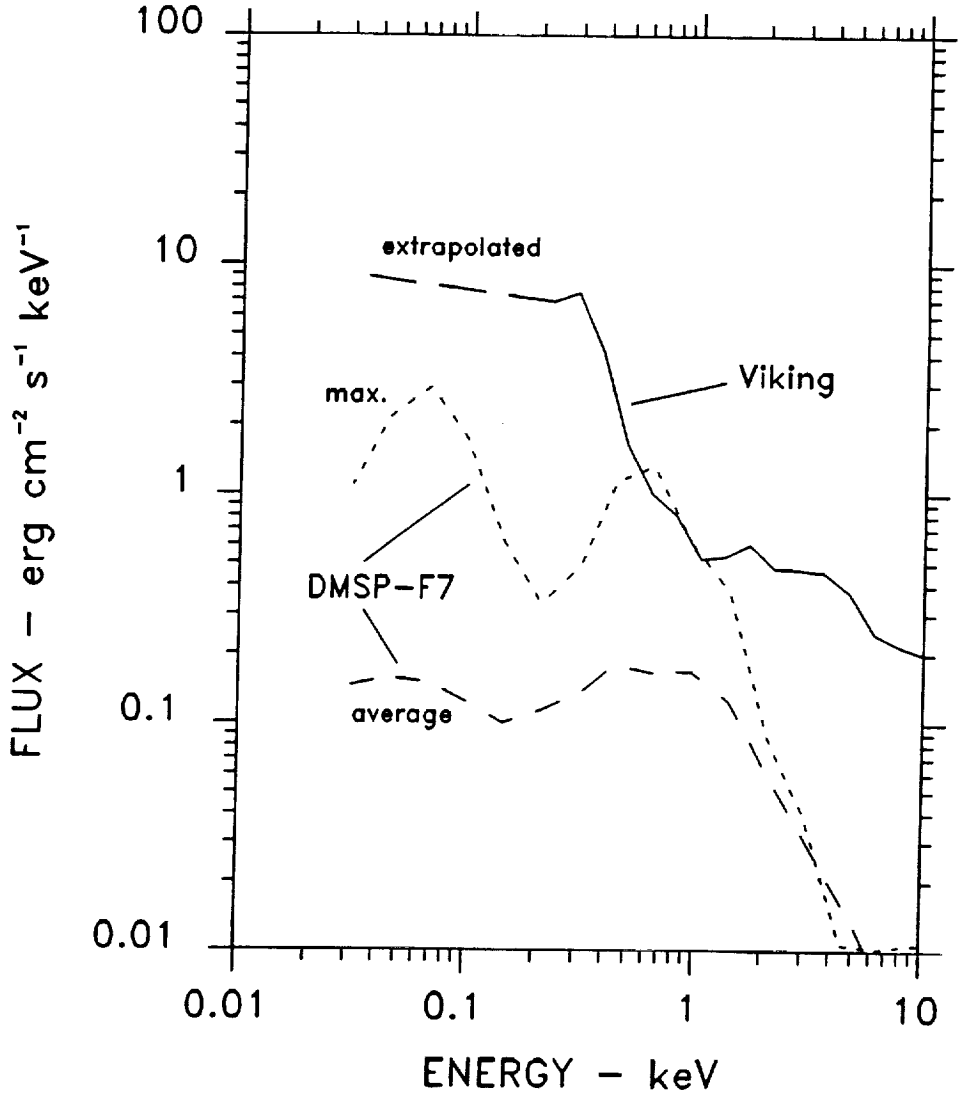
100
10
1
0.1
0.01
0.01
0.1
1
10
FLUX – erg cm⁻² s⁻¹ keV⁻¹
ENERGY – keV
extrapolated
Viking
max.
DMSP-F7
average

Fig. 6

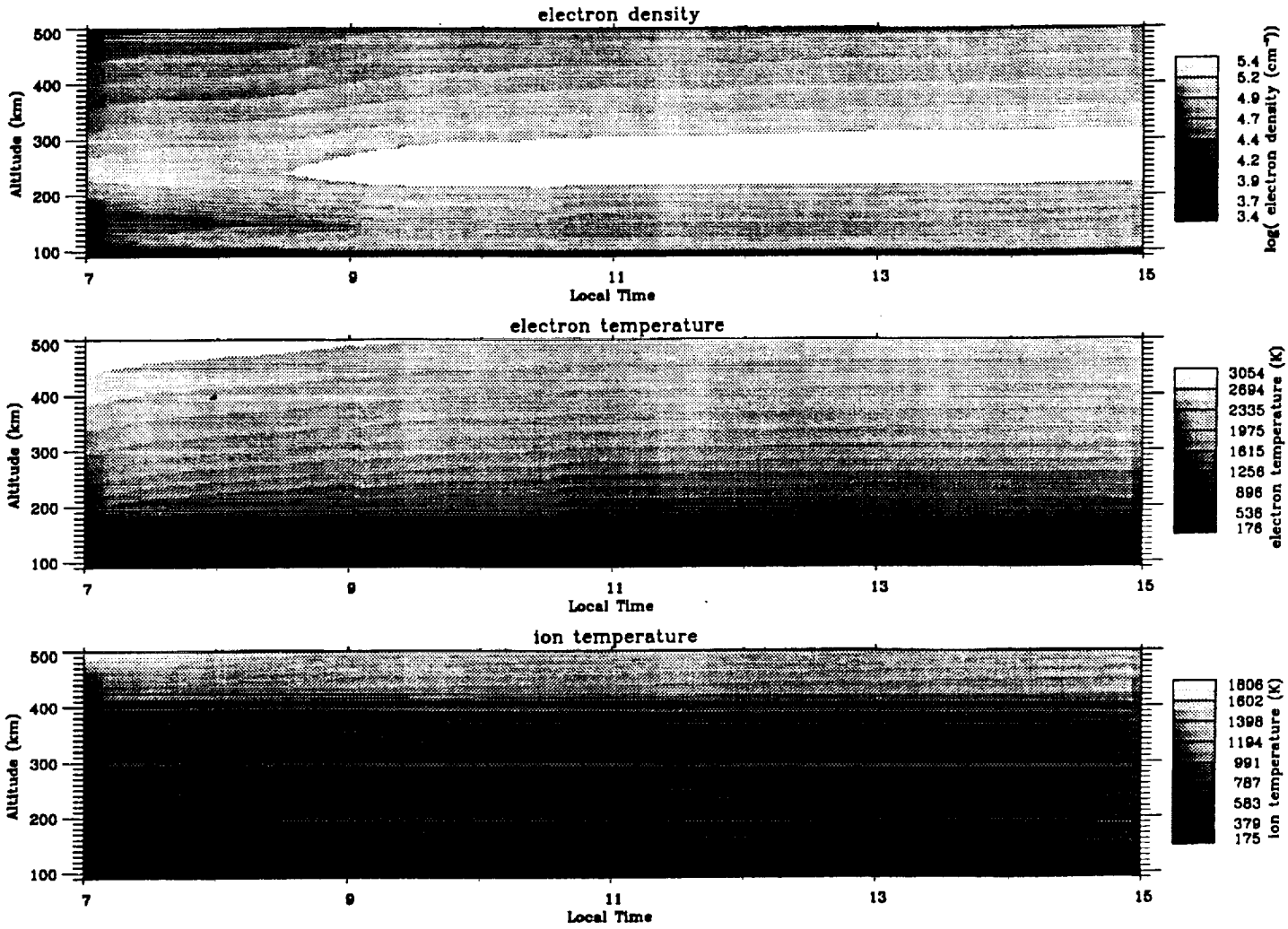
electron density
Altitude (km)
500
400
300
200
100
7
9
11
13
15
Local Time
5.4
5.2
4.9
4.7
4.4
4.2
3.9
3.7
3.4
log(electron density (cm⁻³))
electron temperature
Altitude (km)
Local Time
3054
2694
2335
1975
1615
1256
896
536
176
electron temperature (K)
ion temperature
Altitude (km)
Local Time
1806
1602
1398
1194
991
787
583
379
175
ion temperature (K)

Fig. 7a

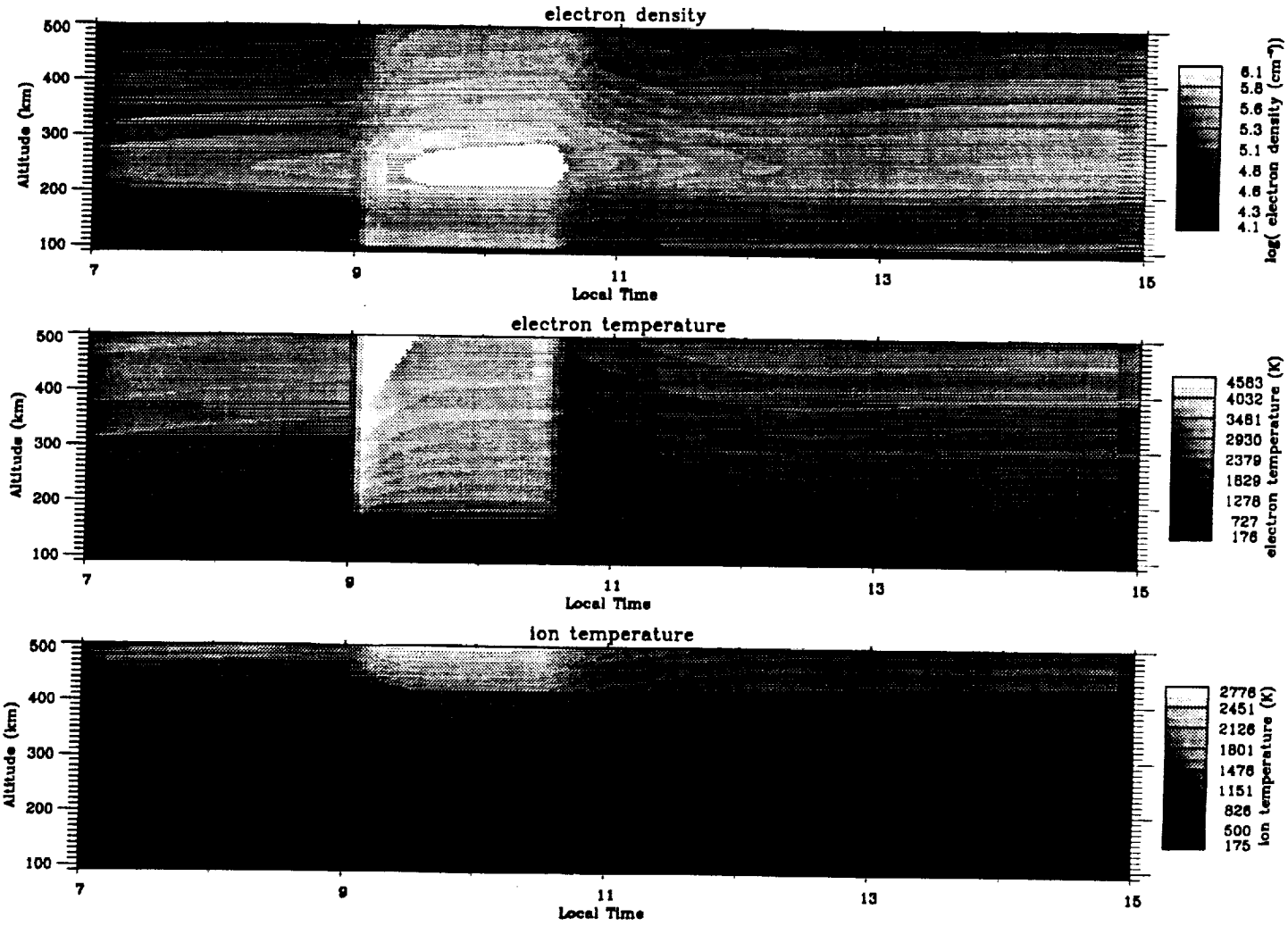
electron density
Altitude (km)
500
400
300
200
100
7
9
11
13
15
Local Time
6.1
5.8
5.6
5.3
5.1
4.8
4.6
4.3
4.1
log(electron density (cm⁻³))
electron temperature
4583
4032
3481
2930
2379
1829
1278
727
176
electron temperature (K)
ion temperature
2776
2451
2126
1801
1476
1151
826
500
175
ion temperature (K)

Fig. 76

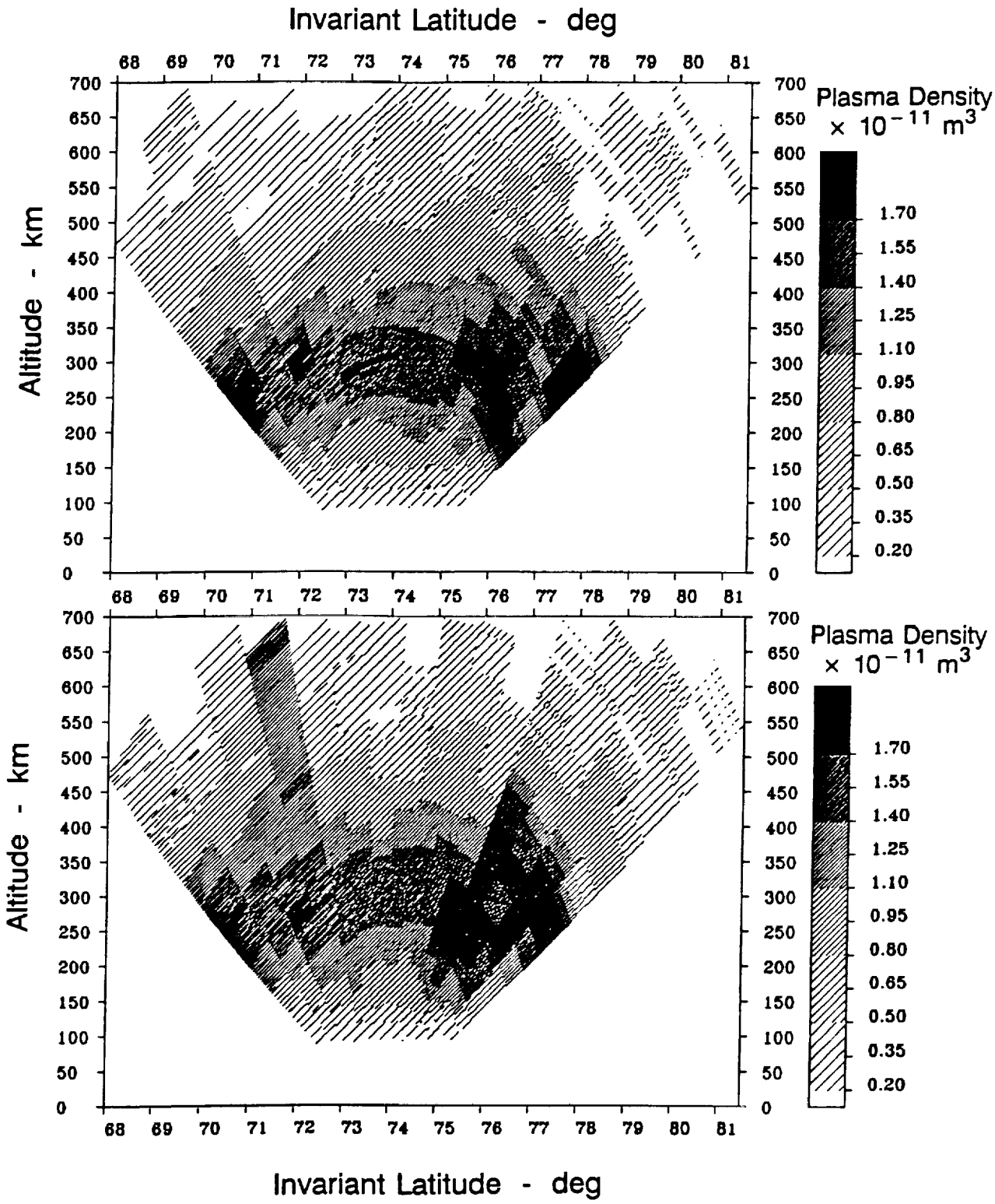
Invariant Latitude - deg
68 69 70 71 72 73 74 75 76 77 78 79 80 81
Altitude - km
700 650 600 550 500 450 400 350 300 250 200 150 100 50 0
Plasma Density
× 10⁻¹¹ m³
1.70
1.55
1.40
1.25
1.10
0.95
0.80
0.65
0.50
0.35
0.20
Plasma Density
× 10⁻¹¹ m³
Altitude - km
Invariant Latitude - deg

Fig. 8

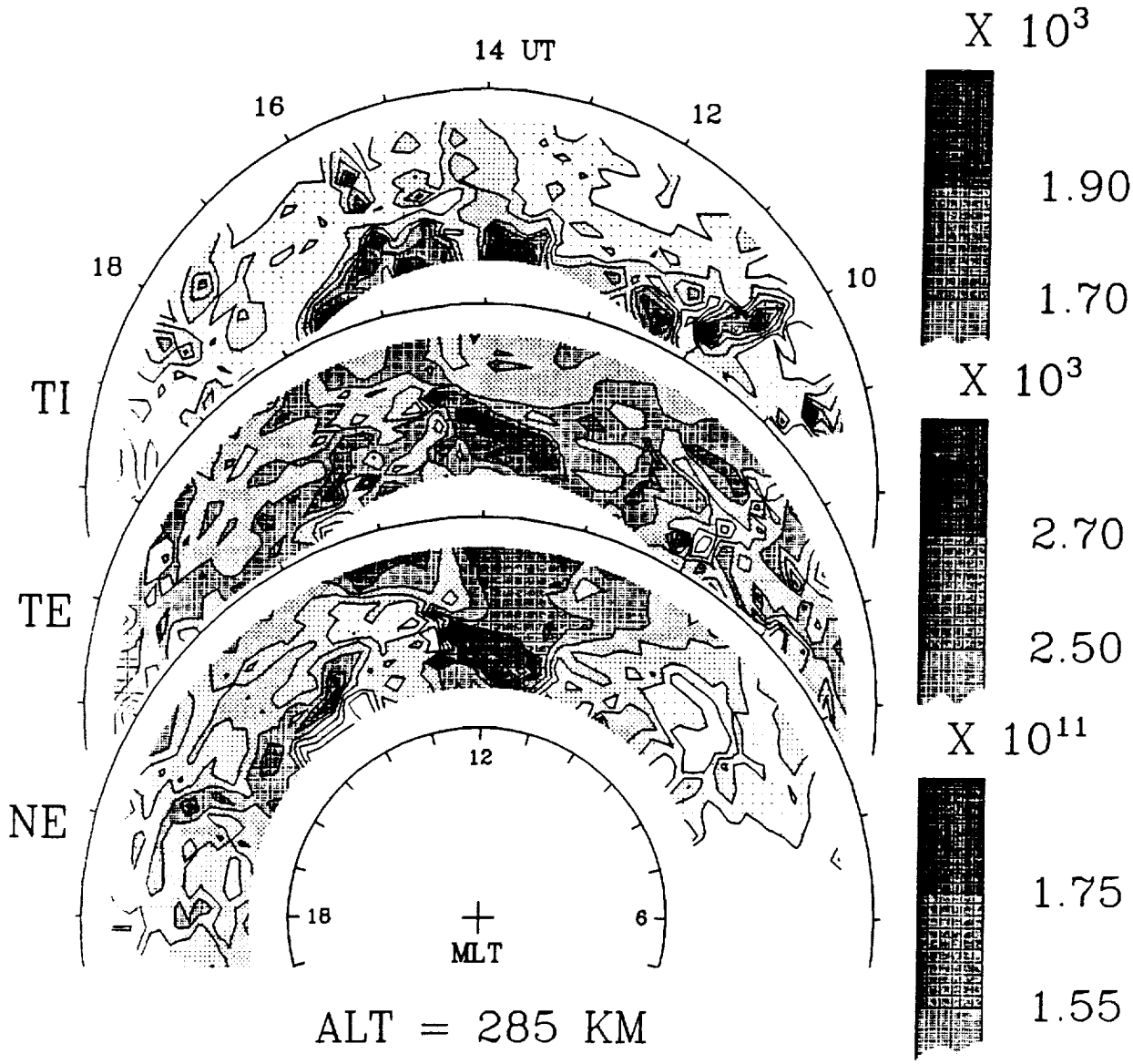

ALT = 285 KM

SONDRESTROM

Fig. 9

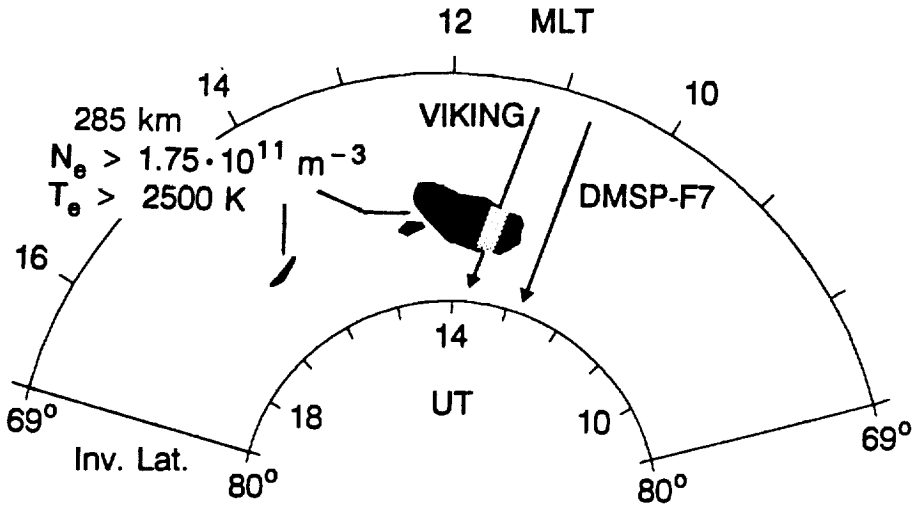
12 MLT
14
10
285 km
$N_e > 1.75 \cdot 10^{11}\ m^{-3}$
$T_e > 2500$ K
VIKING
DMSP-F7
16
14
UT
18
10
69°
Inv. Lat.
80°
80°
69°

Fig. 10

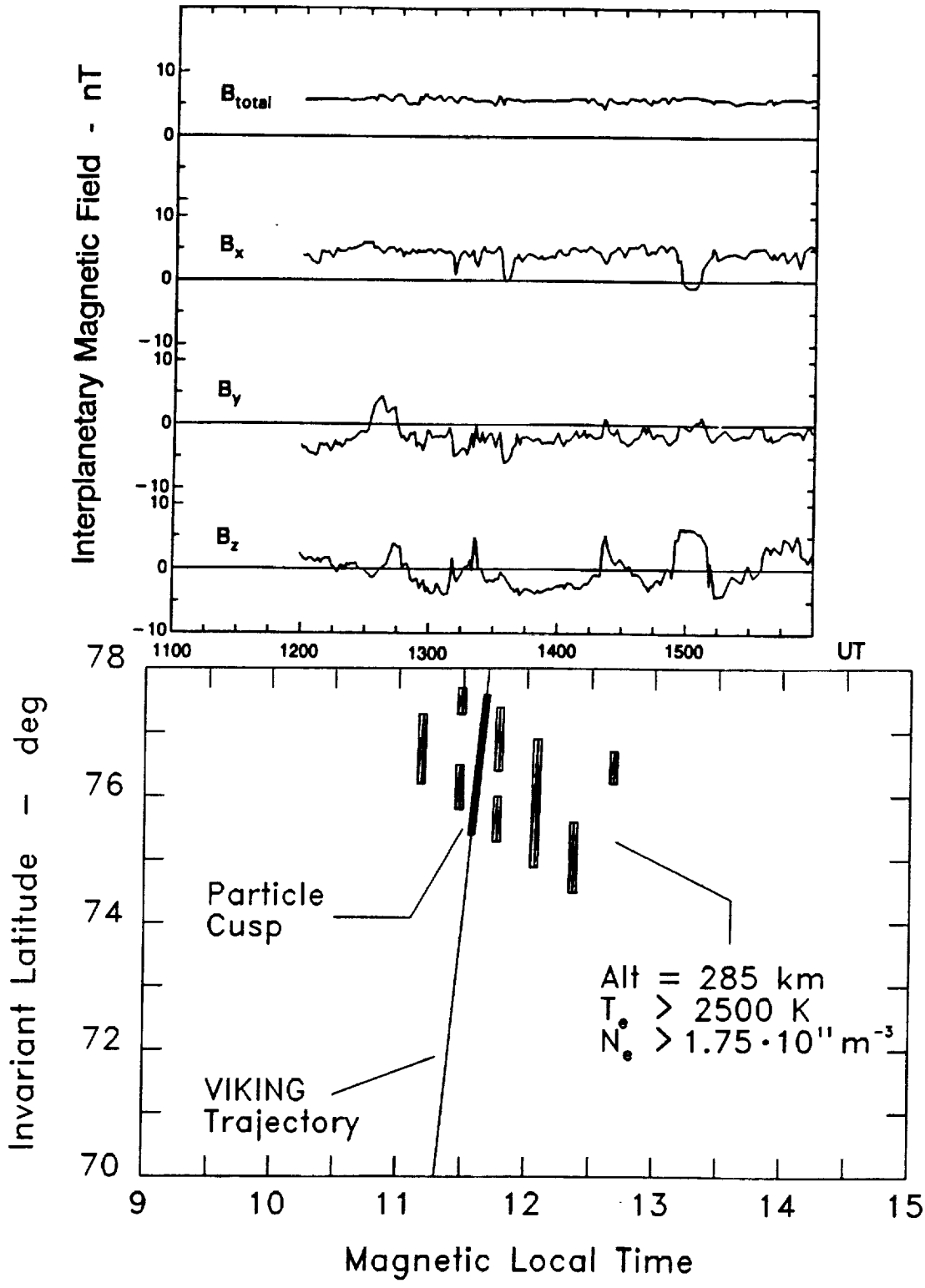
Interplanetary Magnetic Field - nT
B_{total}
B_x
B_y
B_z
10
0
-10
1100
1200
1300
1400
1500
UT
Invariant Latitude - deg
78
76
74
72
70
Particle Cusp
VIKING Trajectory
Alt = 285 km
T_e > 2500 K
N_e > 1.75·10^{11} m^{-3}
9
10
11
12
13
14
15
Magnetic Local Time

Fig. 11

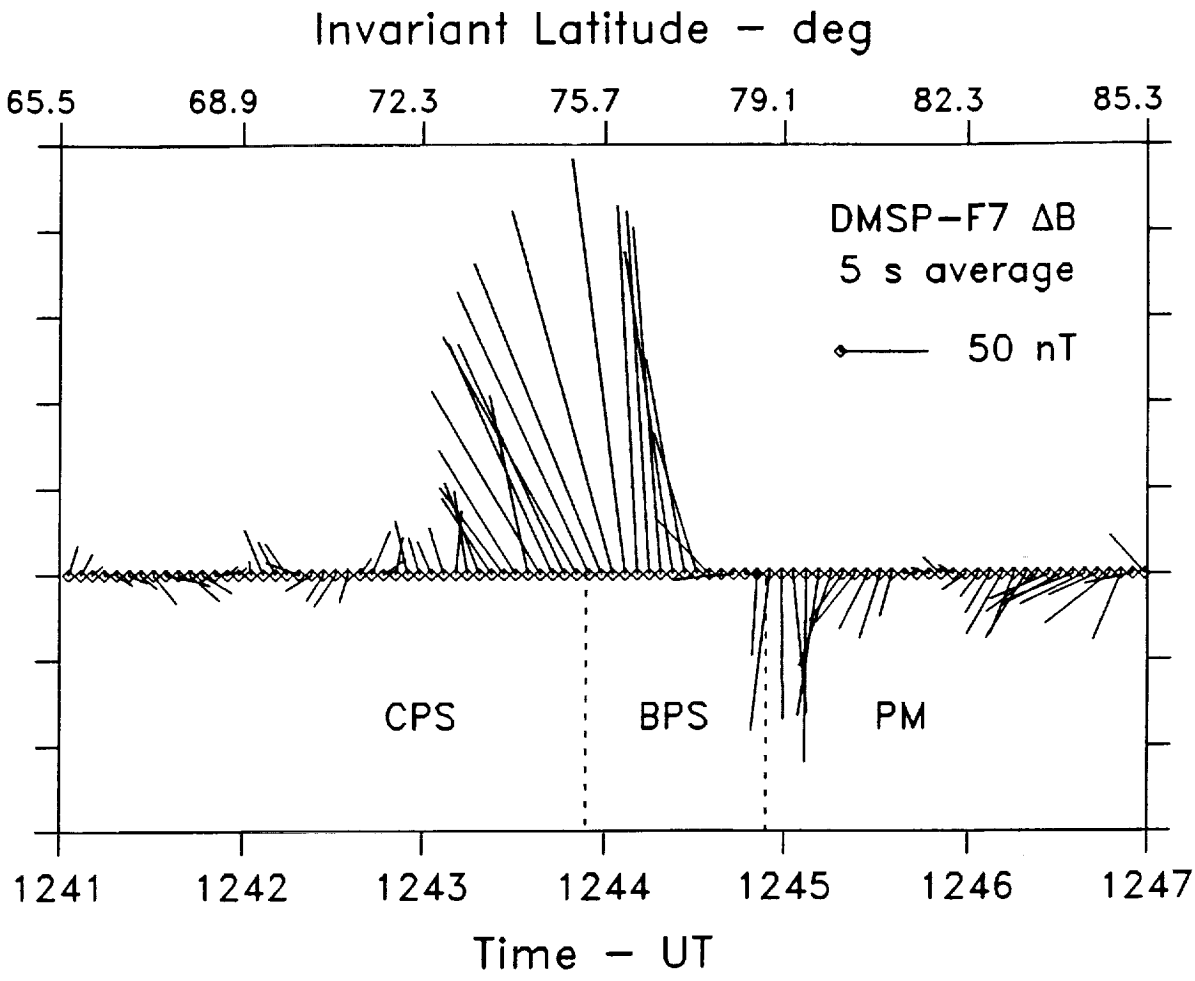
Invariant Latitude – deg
65.5
68.9
72.3
75.7
79.1
82.3
85.3
DMSP–F7 ΔB
5 s average
50 nT
CPS
BPS
PM
1241
1242
1243
1244
1245
1246
1247
Time – UT

Fig. 12a

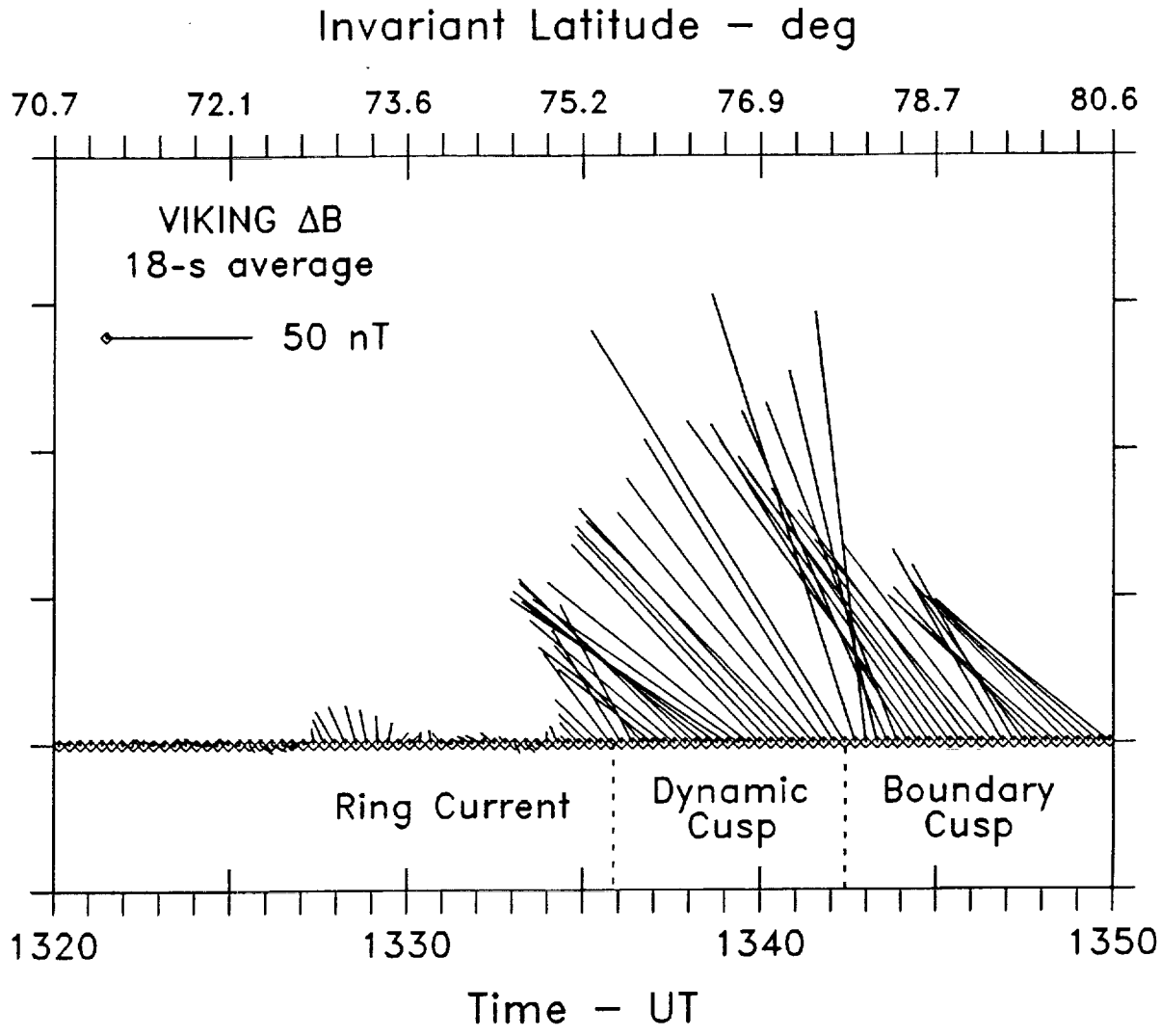
Invariant Latitude – deg
70.7
72.1
73.6
75.2
76.9
78.7
80.6
VIKING ΔB
18-s average
50 nT
Ring Current
Dynamic Cusp
Boundary Cusp
1320
1330
1340
1350
Time – UT

Fig. 12b

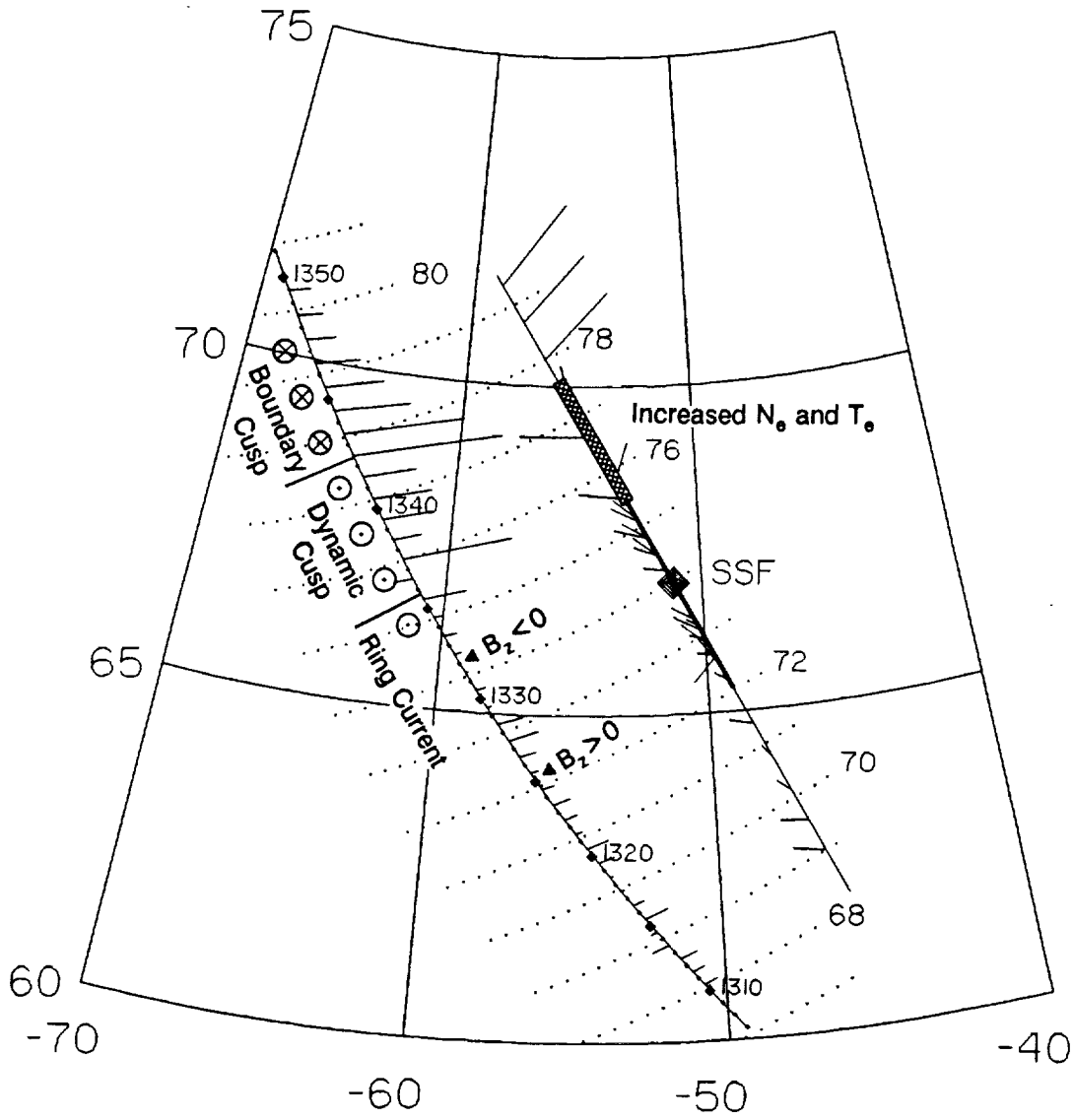
75
70
65
60
-70
-60
-50
-40
80
78
76
72
70
68
1350
1340
1330
1320
1310
Boundary Cusp
Dynamic Cusp
Ring Current
Increased N_e and T_e
SSF
$B_z<0$
$B_z>0$

Fig. 13